

## Single-shot K-Edge subtraction X-ray discrete computed tomography with a polychromatic source and the Pixie-III detector

This is the peer reviewed version of the following article:

*Original:*

Brun, F., Di Trapani, V., Albers, J., Sacco, P., Dreossi, D., Brombal, L., et al. (2020). Single-shot K-Edge subtraction X-ray discrete computed tomography with a polychromatic source and the Pixie-III detector. PHYSICS IN MEDICINE AND BIOLOGY, 65(5) [10.1088/1361-6560/ab7105].

*Availability:*

This version is available <http://hdl.handle.net/11365/1092087> since 2020-02-04T09:53:00Z

*Published:*

DOI: <http://doi.org/10.1088/1361-6560/ab7105>

*Terms of use:*

Open Access

The terms and conditions for the reuse of this version of the manuscript are specified in the publishing policy. Works made available under a Creative Commons license can be used according to the terms and conditions of said license.

For all terms of use and more information see the publisher's website.

(Article begins on next page)

## ACCEPTED MANUSCRIPT

# Single-shot K-Edge subtraction X-ray discrete computed tomography with a polychromatic source and the Pixie-III detector

To cite this article before publication: Francesco Brun *et al* 2020 *Phys. Med. Biol.* in press <https://doi.org/10.1088/1361-6560/ab7105>

## Manuscript version: Accepted Manuscript

Accepted Manuscript is "the version of the article accepted for publication including all changes made as a result of the peer review process, and which may also include the addition to the article by IOP Publishing of a header, an article ID, a cover sheet and/or an 'Accepted Manuscript' watermark, but excluding any other editing, typesetting or other changes made by IOP Publishing and/or its licensors"

This Accepted Manuscript is © 2020 Institute of Physics and Engineering in Medicine.

During the embargo period (the 12 month period from the publication of the Version of Record of this article), the Accepted Manuscript is fully protected by copyright and cannot be reused or reposted elsewhere.

As the Version of Record of this article is going to be / has been published on a subscription basis, this Accepted Manuscript is available for reuse under a CC BY-NC-ND 3.0 licence after the 12 month embargo period.

After the embargo period, everyone is permitted to use copy and redistribute this article for non-commercial purposes only, provided that they adhere to all the terms of the licence <https://creativecommons.org/licenses/by-nc-nd/3.0>

Although reasonable endeavours have been taken to obtain all necessary permissions from third parties to include their copyrighted content within this article, their full citation and copyright line may not be present in this Accepted Manuscript version. Before using any content from this article, please refer to the Version of Record on IOPscience once published for full citation and copyright details, as permissions will likely be required. All third party content is fully copyright protected, unless specifically stated otherwise in the figure caption in the Version of Record.

View the [article online](#) for updates and enhancements.

Single-shot K-Edge Subtraction X-ray discrete  
Computed Tomography with a polychromatic  
source and the Pixie-III detector

Francesco Brun<sup>1,2</sup>, Vittorio Di Trapani<sup>3,4</sup>, Jonas Albers<sup>5</sup>,  
Pasquale Sacco<sup>6</sup>, Diego Dreossi<sup>7</sup>, Luca Brombal<sup>8,2</sup>,  
Luigi Rigon<sup>8,2</sup>, Renata Longo<sup>8,2</sup>, Alberto Mittone<sup>9†</sup>,  
Christian Dullin<sup>5</sup>, Alberto Bravin<sup>9</sup>, and Pasquale Delogu<sup>3,4</sup>

<sup>1</sup> Department of Engineering and Architecture, University of Trieste (Trieste, Italy)

<sup>2</sup> National Institute for Nuclear Physics (INFN), Trieste Division, Italy

<sup>3</sup> Department of Physical Sciences, Earth and Environment, University of Siena (Siena, Italy)

<sup>4</sup> National Institute for Nuclear Physics (INFN), Pisa Division, Italy

<sup>5</sup> Institute for Diagnostic and Interventional Radiology, University Medical Center Goettingen (Goettingen, Germany)

<sup>6</sup> Department of Life Sciences, University of Trieste (Trieste, Italy)

<sup>7</sup> Elettra - Sincrotrone Trieste S.C.p.A., Basovizza (Trieste), Italy

<sup>8</sup> Department of Physics, University of Trieste (Trieste, Italy)

<sup>9</sup> European Synchrotron Radiation Facility (ESRF), Grenoble, France

E-mail: fbrun@units.it

**Abstract.** K-Edge Subtraction (KES) imaging is a technique able to map a specific element such as e.g. a contrast agent within the tissues, by exploiting the sharp rise of its absorption coefficient at the K-Edge energy. Whereas mainly explored at synchrotron radiation sources, the energy discrimination properties of modern X-ray Photon Counting Detectors (XPCDs) pave the way for an implementation of single-shot KES imaging with conventional polychromatic sources. In this work we present an X-ray CT imaging system based on the innovative Pixie-III detector and discrete reconstruction. The results reported here show that a reliable automatic localization of Barium (above a certain concentration) is possible with a few dozens of tomographic projections for a volume having an axial slice of 512×512 pixels. The final application is a routine high-fidelity 3D mapping of a specific element ready for further morphological quantification by means of X-ray CT with potential promising applications *in vivo*.

Keywords: spectral imaging, photon counting detector, computed tomography, discrete reconstruction, contrast agent.

† Present address: CELLS, ALBA synchrotron, Cerdanyola del Valls, Spain.

## 1. Introduction

The K-edge Subtraction (KES) X-ray imaging technique exploits the sharp rise of the absorption coefficient at the K-edge of a specific element such as e.g. an injected contrast agent or a known substance already present in the tissues to be imaged. This technique requires the acquisition of two digital images at different energies at either side of the K-edge of the element to be detected and it can be applied to planar radiography as well as to computed tomography (CT). The logarithmic subtraction of these “low” and “high” energy images enhances the presence of the element (e.g. the structures filled with a contrast agent), whereas the other structures have negligible (or negative) contrast, due to the small variation of their attenuation coefficients at the two considered energies. Image segmentation becomes therefore trivial and automatized, because a global gray level thresholding with a threshold  $t$  slightly above the background noise — such as e.g.  $t \geq 3\sigma$  where  $\sigma$  is the standard deviation of the gray levels in a background region-of-interest (ROI) — gives adequate results.

The tunable monochromatic X-ray beam produced by a synchrotron radiation (SR) source brings the experimental KES performances close to the theoretical limits in terms of image quality [1]. The technique is quantitative and it allows for the detection of very subtle concentrations of a known element with limited radiation dose [2]. However, the scarce availability of suitable SR sources limits a broad application of this technique and therefore KES imaging with non-synchrotron sources is of great interest [3]. Since a conventional X-ray tube has a polychromatic spectrum, it would be desirable to obtain spectral or multi-energy images [4] in a single shot by separating the spectrum in at least two parts (below and above the K-edge of an element). X-ray Photon Counting Detectors (XPCDs) [5][6] which are equipped with a real time multi-threshold discrimination system are capable of acquiring perfectly co-registered data over multiple energy bins in a single scan.

The potential applications of spectral imaging are well known [4], such as e.g. virtual monochromatic imaging, virtual non-contrast exams and scans with much lower doses of contrast medium. Unlike dual energy systems (dual source or tube voltage switching), photon-counting spectral imaging eliminates the risk of misregistration between the energy images thanks to its single-shot nature. However, whereas spectral imaging with XPCDs is considered very promising, its practical application has been hampered by the charge sharing problem [5] that negatively affects the energy resolution of these detectors. Additional technological problems affect the quality of the acquired images, thus leading to the need of accurate digital image processing procedures [7] in order to compensate for noise and artifacts.

Based on simulations using solutions containing different concentrations of gadolinium and iodine [8, 9], K-Edge computed tomography with XPCDs has been already proved to be a promising technique to map contrast agents in tissues. CdTe detectors are the most widely used solution in this field [10] and several optimizations have been presented through the last decade [11, 12].

This work presents the single-shot K-Edge Subtraction Computed Tomography (KES-CT) technique where the innovative Pixie-III detector [13][14] is used combined with discrete reconstruction. Pixie-III allows to configure two programmable energy thresholds and it implements a solution to cope with charge sharing effects, thus allowing to collect two images simultaneously with sharp energy (or color) sensitivity. These two images are here combined with refined image processing as well as a state-of-the-art discrete tomography [15] [16] reconstruction algorithm named Total

Variation Regularized - Discrete Algebraic Reconstruction Technique (TVR-DART) [17]. KES imaging is meant mainly to ease segmentation and further morphological quantification. This is beneficial for example in the 3D visualization of the vascular system of small animals [18–20]. For a detailed morphological quantitative analysis of the vascular tree, it is necessary to reconstruct the vascular network in its entirety and a binary segmented volume is required to quantify e.g. the vessel length and caliber in order to characterize a small artery occlusion and compression [19]. When considering the CT case, due to the inherent amount of noise and artifacts of PCXDs, it might be hard to segment the KES image if a conventional gray-level tomographic reconstruction with subsequent thresholding is applied. Discrete tomography could be beneficial in this case, since it focuses on the reconstruction of objects that consist of only a few different materials. Ideally, a CT reconstruction of such a sample should contain only one gray level for each of its components. By exploiting this property within the reconstruction algorithm, the produced images typically contain fewer artifacts since gray levels are concentrated towards a limited number of values or strictly enforced towards only two gray values, so to ease the separation of the background from the features of interest. Thanks to this, a limited number of projections is usually enough to produce adequate images and this in principle favors a reduction of the delivered radiation dose or the acquisition time.

In order to verify the performances of the Pixie-III detector for KES tomographic imaging with polychromatic sources, the localization of clusters of Barium nanoparticles in a breast cancer mouse model is considered in this work. Breast cancer is the most common cancer in women worldwide and nanoparticles can enhance the contrast for further imaging. In addition, it is speculated that nanoparticles might enhance the efficiency of radiation therapy, due to their X-ray absorbing characteristics, which can increase the local radiation dose while lowering undesired dose deposition [21].

Preliminary results were already reported in [22,23] where test objects were used and in [24,25], where the benefits of the energy resolution of the Pixie-III detector were assessed. The quantification of Ba nanoparticles in a breast cancer mouse model reported in this article is validated against a reference image acquired at a synchrotron radiation source. The final result is an effective lab-based technology for an automated 3D mapping of a specific element.

2. Materials and Methods

2.1. Test objects

Three different polypropylene 350  $\mu$ l small tubes were prepared: one filled with an Iodine-based solution (Bayern Ultravist©— 93 mg/ml), a second one filled with a BaCl<sub>2</sub> (Carlo Erba Reagents — 122 mg/ml) solution and another one filled with de-ionized water. The K-Edge value for I is 33.2 keV and for Ba is 37.4 keV. This simple test object was first considered to optimize the values of the detector energy thresholds by analyzing simple planar radiographic images. A sketch of this test object is reported in Fig. 1. Then a second test object composed of polypropylene 350  $\mu$ l small tubes filled with different dilutions of BaCl<sub>2</sub> (Carlo Erba Reagents) and de-ionized water was prepared. It was designed to be considered for CT imaging in order to assess the minimum detectable concentration of Ba. A sketch of this second test object with the considered dilutions of BaCl<sub>2</sub> with water is reported in Fig. 2.

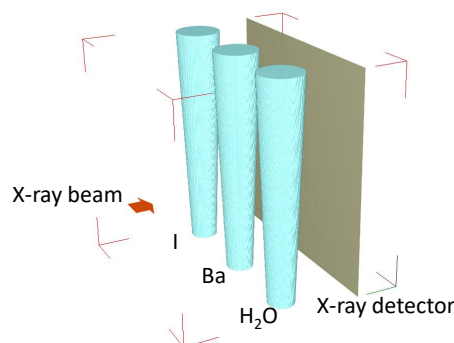


**Figure 1.** Sketch of the test object used to optimize the settings of the detector energy thresholds by considering planar radiographs. It is composed of three pipettes filled with: an I-based (Bayern Ultravist© — 93 mg/ml) solution; a  $\text{BaCl}_2$  (Carlo Erba Reagents — 122 mg/ml) solution and a reference small tube filled with deionized water. [Ba K-edge = 37.4 keV, I K-edge = 33.2 keV].

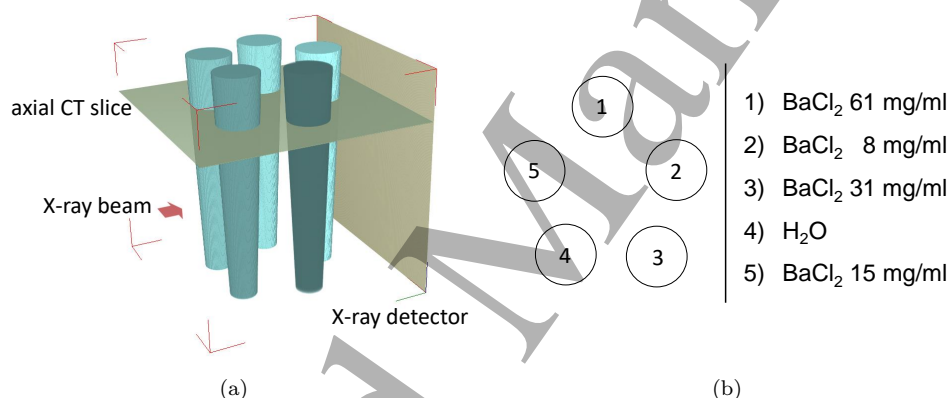


**Figure 2.** a) Sketch of the test object prepared for CT imaging and used to assess the minimum detectable concentration of Ba. b) Order and composition of the considered pipettes as will result from an axial CT slice.

## 2.2. Biomedical sample

Tumor growth is induced by the injection of  $1 \times 10^6$  H8N8 breast cancer cells directly into the breast tissue of a female WAP-T mouse. The mouse has been sacrificed 4 weeks after injection of the tumor cells. Barium nanoparticles were injected directly into the tumor one day before sacrificing the mouse. The tumor and the surrounding tissue were excised, fixated and embedded in a standard paraffin block commonly used for histological analysis. All animal procedures were performed in accordance with European guidelines (2010/63/EU) and approved by the corresponding ethics institutions (administration of Lower Saxony, Germany, license No. 33.9-42502-04-18/3022)

### 2.3. SR $\mu$ -CT acquisition and reconstruction

Synchrotron Radiation (SR) imaging was performed at ID17 beamline of the European Synchrotron Radiation Facility (ESRF, Grenoble - France) in order to take advantage of a high flux X-ray beam monochromatized thanks to a double Si(111) Laue monochromator [26]. Monochromatic settings at 36.5 keV and 38.5 keV, respectively were applied for the KES CT image acquisition. A PCO-Edge 5.5 camera (detector pixel size =  $6.5 \times 6.5 \mu\text{m}^2$ ) was used in combination with a 1:1 optics [27]. The exposure time was 50 ms and 2,000 projections were collected. Parallel beam filtered back projection reconstruction was applied to get the reconstructed volume at a voxel size of  $6.5 \times 6.5 \times 6.5 \mu\text{m}^3$ . The high-resolution volume will be further used in future studies where a comparison with histology will be performed. In this application, it was down-scaled with averaging to produce a high-quality reference image having a nominal voxel size of  $52 \times 52 \times 52 \mu\text{m}^3$ , ready to further registration and comparison with the lab-based image. A ROI of the registered image is reported in Fig. 3 together with its segmentation by thresholding.

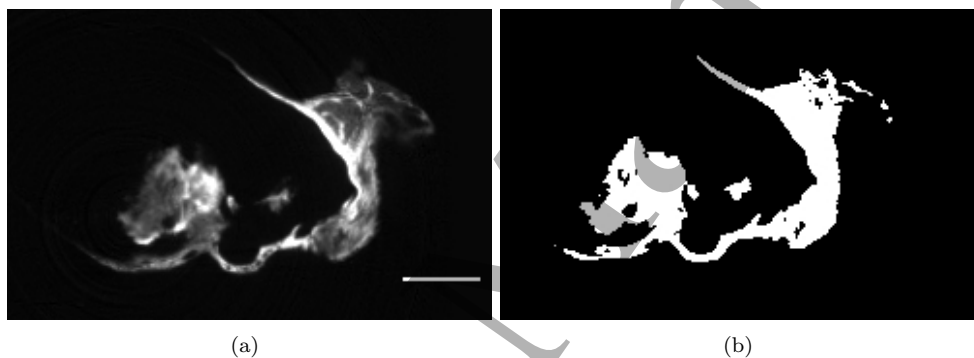


**Figure 3.** ROI of the (a) registered SR-KES reference image and (b) its segmentation. The considered gray level threshold was computed as the  $t = 5\sigma$  where  $\sigma$  is the standard deviation of the gray levels in the background. [The scale bar is 2 mm]

### 2.4. KES laboratory imaging setup

A micro-focus Hamamatsu X-ray source (tube voltage: 20 to 90 kV, tube current: 0 to 200  $\mu\text{A}$ , maximum output: 8 W, focal spot size:  $5 \mu\text{m}$ ) and a CdTe Pixirad-I/Pixie-III detector [13, 14] (sensitive area:  $31.7 \times 25.0 \text{ mm}^2$  organized as a  $512 \times 402$  pixels on a square matrix at  $62 \mu\text{m}$  pitch) were used. The detector was configured in Neighbor Pixel Inhibit - Pixel Summing Mode (NPISUM) [24]: in this case the hit event is allocated to the pixel receiving the highest fraction of the total deposited energy and after that the signals of the pixels in the 4-connected neighborhood are summed up to correctly evaluate the total energy.

The linearity of the Pixirad-I detector (mainly limited by the dead time of the electronics) has been already investigated [28] by varying the impinging photon up to its paralyzation. The results indicate that the system remains linear up to  $1 \times 10^5$  counts per pixel per second. Information about the energy response, i.e. the ratio between detector counts and number of impinging photons, as a function of energy

and of discriminator thresholds, is also reported in [28]. Moreover, noise and efficiency of Pixie-III has been assessed in [24] where the benefits of the NPISUM mode are discussed. In addition, the energy resolution of Pixie-III with the NPISUM mode varies from 13.0% to 8.2% in the range 26 keV - 50 keV [25].

Thanks to its two programmable energy thresholds  $E_{\text{low}}$  and  $E_{\text{high}}$ , the detector outputs in a single exposure two images (see Figure 6), hereafter referred as to “low” (in the energy range  $[E_{\text{low}}, E_{\text{high}}]$ ) and “high” (in the range  $[E_{\text{high}}, +\infty]$ ). The logarithmic digital subtraction of the two images is then performed to get the KES image, i.e. an image where only the desired element is supposed to give strictly positive gray levels. More precisely, this image is the difference of the logarithms of the (normalized) photon counts, i.e.  $I_{KES} = \log(I_{K+}) - \log(I_{K-})$ , where  $I_{K+}$  and  $I_{K-}$  are the (flat-corrected) acquired “high” and “low” images, respectively.

### 2.5. KES-CT laboratory imaging: geometry, pre-processing and reconstruction

The parameters used in the cone-beam CT geometry are: distance source-to-object  $D_{\text{SO}} = 200$  mm, distance source-to-detector  $D_{\text{SD}} = 250$  mm, 720 projections over 360 degrees in “step and go” mode with 10 repetitions per angle. The inherent magnification of the cone beam geometry gives a nominal voxel size of the reconstructed images of approximately  $50 \times 50 \times 50 \mu\text{m}^3$ .

Since 10 repetitions were collected, three different datasets were derived in order to simulate different acquisition statistics. In a first case, the 10 repeated images were averaged. In the second case, only 5 images were considered for the averaging. A single image (no averaging) was also considered for a third “low statistics” dataset. Similarly, to simulate different angular sampling, projections were decimated to a factor 4 (i.e. 180 projections) and 12 (i.e. 60 projections), respectively. Thus, in total, 9 different acquisition protocols were considered.

Due to limitations of the charge recovery hardware algorithm of Pixie-III, a few unpredictable hot/dead pixels were observed in the acquired projection and they have to be handled before the reconstruction process since they would produce severe streak and ring artifacts. A custom automatic detection and removal non-linear filter was used to compensate for these defective pixels. This filter considers a  $5 \times 5$  neighborhood and its median gray value  $m$ . If the absolute difference between the gray-level of the central pixel and  $m$  is above a user-specified fixed threshold  $\delta$ , the value of the central pixel is then replaced. The replaced value is not  $m$  but it is the median of the set composed by the pixels that satisfy the previous condition, i.e. having the absolute difference between their gray level and  $m$  below the threshold.

Since ring artifacts in the final reconstructed images might still occur, effective ring removal solutions were included. After conventional reconstruction of the KES dataset with the cone-beam FDK (Feldkamp, Davis and Kress) [29] algorithm, an implementation of one of the ring removal filters reported in [30] was used. The considered method corrects ring artifacts after tomographic reconstruction and it takes advantage of the observation that ring artifacts become straight vertical lines by transforming the input image into polar coordinates where the center of the ring artifacts is assumed as the center of the Cartesian-to-polar conversion [31]. A de-striping filter [32] is therefore applied prior to the inverse transformation.



## 2.6. Image comparison

The SR reference image (having nominal voxel size of  $52 \times 52 \times 52 \mu\text{m}^3$ ) has been co-registered (affine registration) with respect to the proposed lab-based CT volume reconstructed with FDK having nominal voxel size of  $50 \times 50 \times 50 \mu\text{m}^3$ , in order to propose a voxel-by-voxel quantitative comparison. As mentioned in the introduction, the global gray level threshold has been set to  $t = 3\sigma$  where  $\sigma$  is the standard deviation of the gray levels in a background ROI. Fig. 3 reports this reference image. After that the segmentation error has been evaluated by assessing the number of true positives ( $TP$ ), false positives ( $FP$ ) and false negatives ( $FN$ ) with respect to the SR reference thresholded image. These values were combined in the Jaccard index  $\epsilon = TP / (TP + FP + FN)$ .

## 2.7. Discrete reconstruction

Discrete reconstruction with the TVR-DART [17] algorithm was applied to the proposed lab-based KES image. The code publicly available here: <https://github.com/astra-toolbox/ContributedTools> was used. TVR-DART is capable of providing more accurate reconstruction than existing algorithms under noisy conditions from a small number of projection images and/or from a small angular range [17]. Non-negativity constraints were added in order to get at the end a reconstructed volume where non-zero voxels represent the map of Barium in the considered sample. As done for the conventional reconstruction, 9 different acquisition protocols were considered. The amount of non-zero voxels has been quantified and a segmentation error was determined against the thresholded SR reference image for each of the considered datasets. Again, the the number of  $TP$ ,  $FP$ , and  $FN$ , as well as  $\epsilon$  were determined.

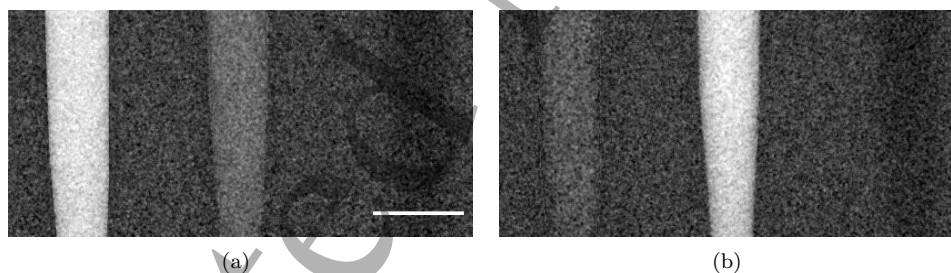


**Figure 4.** KES (flat-corrected) radiographs of the considered test object composed of small tubes filled with a solution of I, Ba and  $\text{H}_2\text{O}$  (see Fig.1). For both images the X-ray source settings are the same, i.e. voltage = 50 kV and 1 mm of Al filter. The detector energy thresholds are: a)  $E_{\text{low}} = 28.0 \text{ keV}$ ,  $E_{\text{high}} = 33.5 \text{ keV}$ ; b)  $E_{\text{low}} = 28.0 \text{ keV}$ ,  $E_{\text{high}} = 38.0 \text{ keV}$ . [The scale bar is 5 mm.]

## 3. Results and discussion

Figure 4 reports two different planar KES images of the test object used for the optimization of the values for the detector energy thresholds. It can be easily noticed that different detector settings produce different KES images with the same input X-ray spectrum. An extremely fine tuning of the X-ray spectrum combined with the

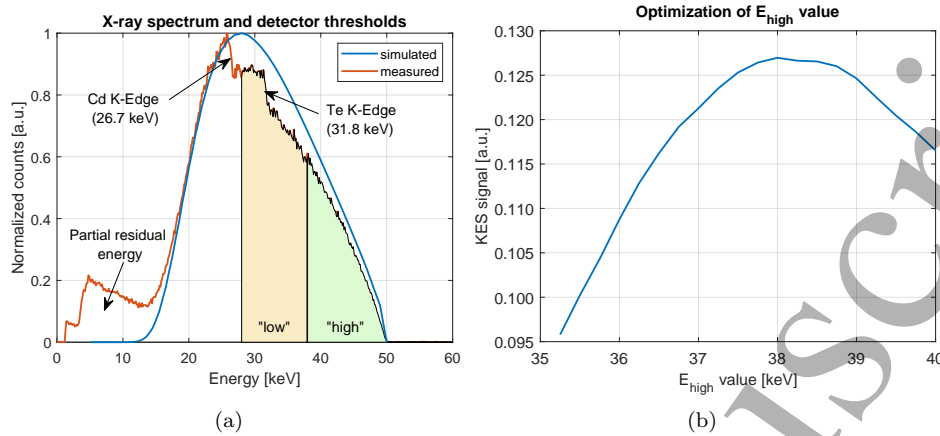


**Figure 5.** (a) Plot of the considered X-ray spectrum with superposition of the adopted detector energy thresholds. (b) Plot of the Contrast-to-Noise Ratio (CNR) of the different planar KES images by considering different values for the detector  $E_{high}$  energy threshold. A ROI within the Ba small tube and a ROI within the background have been considered for the computation of the CNR.

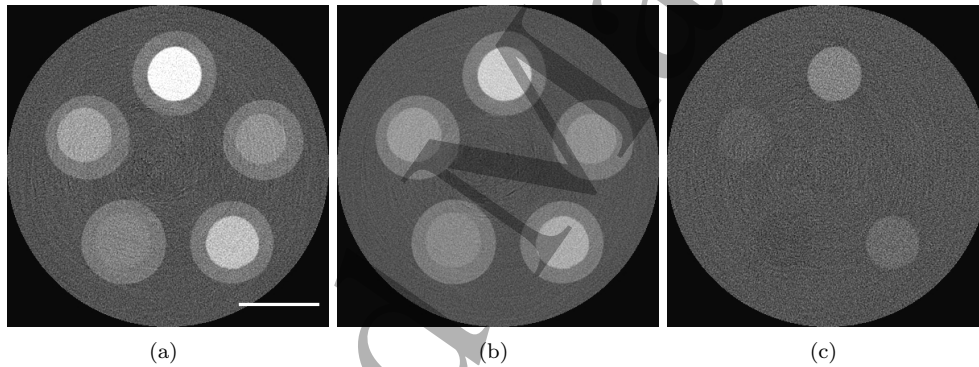


**Figure 6.** Tomographic axial slice (512×512 pixels) of the considered test object for CT (see Fig. 2): a) low-energy image; (b) high-energy image; c) resulting KES image where only the Ba content within the small tubes results highlighted. Resulting isotropic voxel size is  $50 \times 50 \times 50 \mu\text{m}^3$ . The same window/level gray-value settings are used for the three images. [The scale bar is 5 mm]

values for the energy thresholds will be explored with more details in future works, being in general application-dependent. In this work, the maximization of the KES signal was used as the criterion for the selection of the energy thresholds. The following settings result in a reasonable trade-off for the detection of Ba: X-ray tube voltage  $V = 50$  kV, current = 160  $\mu\text{A}$ , 1mm Al filter, exposure time = 1 s, detector energy thresholds  $E_{low} = 28.0$  keV,  $E_{high} = 38.0$  keV. The X-ray spectrum as produced by the considered X-ray tube was first simulated via SpekCalc [33–35]. An experimental measure was performed by means of a CdTe Amptek X-ray spectrometer in order to validate the simulation. Unlike the simulated one, the recorded spectrum is affected by the Cd and Te K-edges, thus better representing the expected behaviour of Pixie-

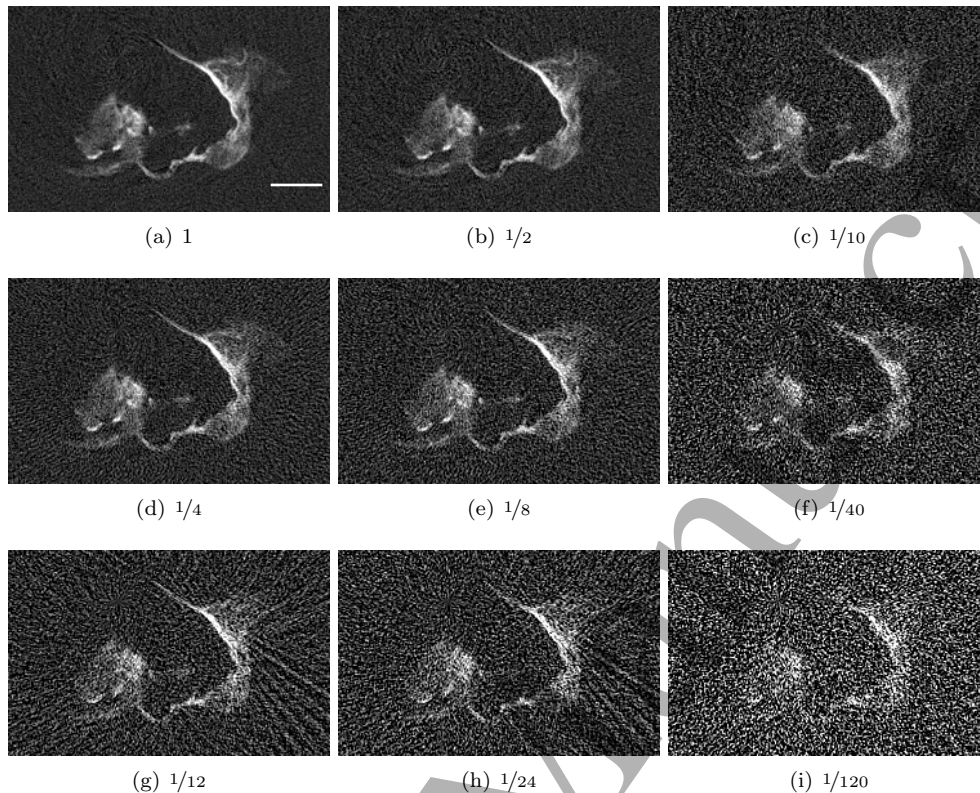


**Figure 7.** ROI of an axial slice of the KES image of the considered biomedical sample reconstructed with conventional FDK when using: (first row - a,b,c) 720 projections; (second row - d,e,f) 180 projections; (third row - g,h,i) 60 projections and (first column - a,d,g) projection averaging with 10 images; (second column - b,e,h) projection averaging with 5 images; (third column - c,f,i) no projection averaging. The reduction factor of the total photon flux with respect to the dataset with highest statistics is reported in each subcaption. [The scale bar is 2 mm]

III. Results are reported in Fig. 5a. The simulation gives an estimated entrance dose of 0.176 mGy at the sample per collected radiograph with the considered setup.

The value for  $E_{\text{low}}$  should be, in principle, close enough to the value of  $E_{\text{high}}$  but an adequate photon statistics is required in the “low” image and therefore it has to be shifted towards lower energies. In this work  $E_{\text{low}} = 28$  keV was assumed as set. Its position was not fine tuned, being less critical than  $E_{\text{high}}$ . The values for  $E_{\text{high}}$  result from the optimization presented in Fig. 5 based on a so-called threshold scan, i.e. different acquisitions with the same  $E_{\text{low}}$  value and increasing  $E_{\text{high}}$  values. The resulting KES images were analyzed by considering a ROI within the Ba small tube. The  $E_{\text{high}}$  value for which the ROI average value resulted maximum was chosen as optimal value. Due to the finite energy resolution of the detector, different criteria for the positioning of  $E_{\text{high}}$  might be adopted. Instead of maximizing the KES signal, a slight shift of  $E_{\text{high}}$  towards higher (or lower) energies might be preferred in order to avoid contamination with materials having a K-edge lower than (or higher than) the

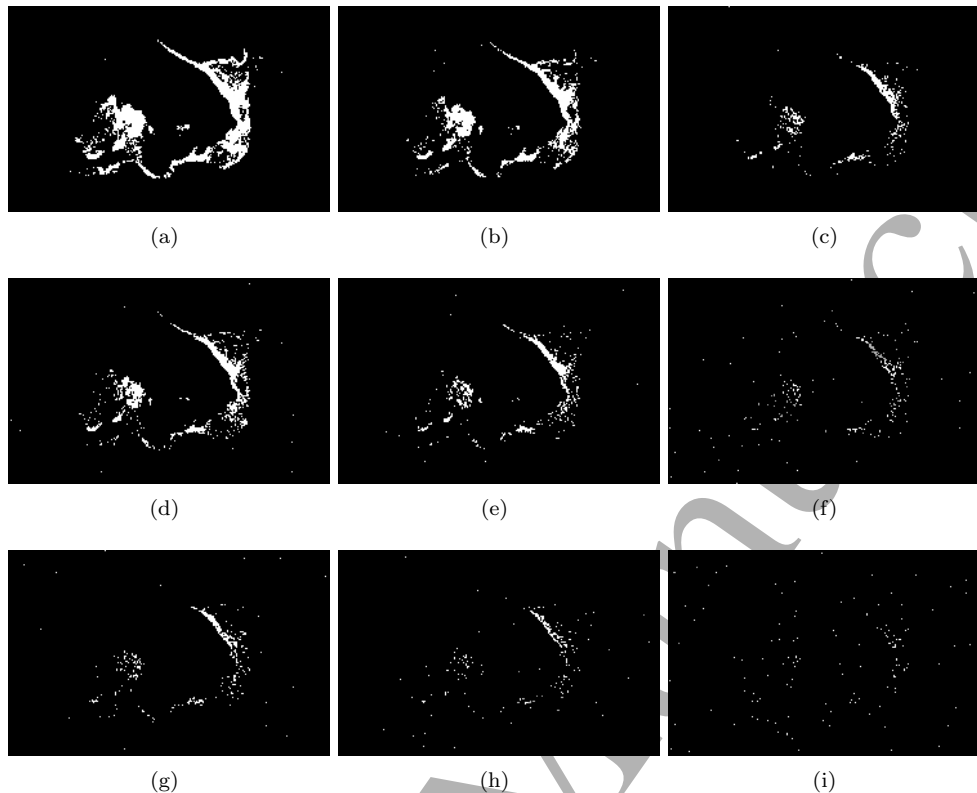


**Figure 8.** ROI of an axial slice of the KES image of the considered biomedical sample after conventional FDK reconstruction and thresholding with threshold  $t = 3\sigma$  where  $\sigma$  is the standard deviation of the gray levels in a background ROI. The segmentation was performed on the FDK reconstructed images when using: (first row - a,b,c) 720 projections; (second row - d,e,f) 180 projections; (third row - g,h,i) 60 projections and (first column - a,d,g) projection averaging with 10 images; (second column - b,e,h) projection averaging with 5 images; (third column - c,f,i) no projection averaging.

target material.

Figure 6 reports an axial slice of the test object used for CT imaging and to assess the minimum detectable concentration of Ba. The images result from the acquisition protocol with the highest statistics (projection averaging over 10 image and 720 projections). The advantages for further image segmentation and quantification are visible in the KES image where only Ba contents give a positive gray-value and all the other elements become indistinguishable from the background (the latter having ideally gray level 0). Although a fine assessment of the minimum detectable concentration of Ba goes beyond the purposes of this article, it is implicit that a localization of Ba contents above a certain concentration is feasible with the proposed settings. It is also reasonable to infer that with higher photon statistics also much lower concentrations of Ba can be identified.

Figure 7 shows a ROI of an axial slice of the lab-based KES images by considering different acquisition statistics. These gray level images can be visually compared

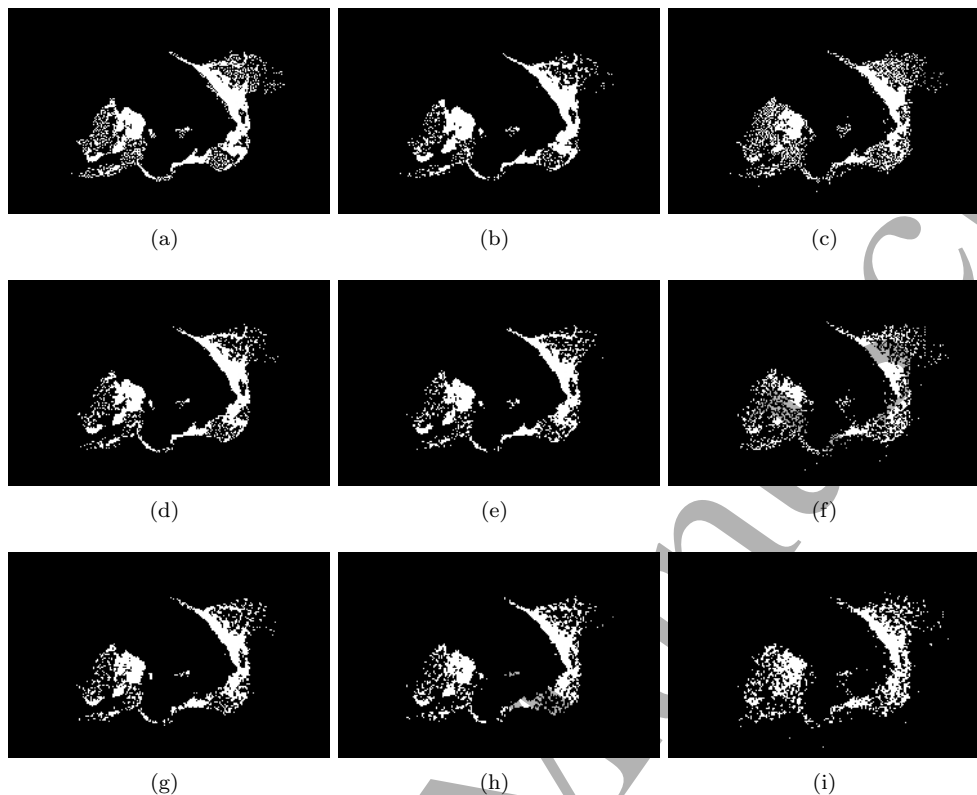


**Figure 9.** ROI of an axial slice of the KES dataset reconstructed with TVR-DART (direct binary reconstruction) when considering: (first row - a,b,c) 720 projections; (second row - d,e,f) 180 projections; (third row - g,h,i) 60 projections and (first column - a,d,g) projection averaging with 10 images; (second column - b,e,h) projection averaging with 5 images; (third column - c,f,i) no projection averaging;

with Fig. 3a where the reference SR (downscaled and registered) KES image is presented. Although a good agreement with the reference image can be visually noticed, a quantitative comparison is required to better comment the differences. The images reported in Fig. 7 have been segmented via thresholding with threshold  $t = 3\sigma$  where  $\sigma$  is the standard deviation of the gray levels in a background ROI. Then, a segmentation error has been evaluated. Figure 8 reports the segmented images and Table 1 presents the results of the quantitative comparison with the SR image.

The results presented in Table 1 show the difficulties of an automated segmentation with threshold  $t = 3\sigma$  (where  $\sigma$  is the standard deviation of the gray levels in a background ROI) when reducing the acquisition statistics. The values for the Jaccard index decrease coherently with the reduction of the statistics. It is worth noticing that these values are far from 1 even for the highest statistic image. This is due to the fact that subtle concentrations of Ba are identified in the ground truth SR image thanks to its extremely high spatial, contrast and energy resolution. These concentrations are hidden by the background noise in the lab-based images. Moreover, the quantitative values are worsened by the unavoidable image registration process

required by this voxel-by-voxel quantitative comparison. It is implicit that other reconstruction algorithms such as iterative approaches might have been considered since they are widely recognized as beneficial in the case of high noise and sparse views. However, many of these require the fine tuning of one or more regularization parameters and/or a proper assessment of the number of iterations. These aspects are in general application-dependent.

In order to go towards a low-dose localization of a specific element, the TVR-DART algorithm has been applied to the considered datasets. Figure 9 reports the same ROI for a reconstructed image (direct binary reconstruction) when considering the different acquisition protocols. The results of the quantitative comparison with the SR image are presented in Table 2. It can be noticed that the values for the Jaccard index fluctuates around an average value when considering all the TVR-DART cases from 720 projections with averaging to the volume reconstructed with 60 angles and without projection averaging. This confirms that TVR-DART is a robust discrete tomography reconstruction method and it performs adequately also when a reduced number of projections is considered.

With the proposed laboratory system based on a conventional X-ray source and the Pixie-III detector, KES imaging is possible and, above a certain concentration, a reliable localization and quantification of a contrast medium is feasible. The performances of the polychromatic KES approach are inferior to those of synchrotron radiation imaging, but the single-shot lab-based nature of the proposed system is a key advantage for all the practical applications where motion artifacts and radiation dose are a concern. When the final goal is a binary map where only the contrast agent results highlighted, lab-based KES imaging combined with discrete tomography is a promising valuable tool. Among the others, TVR-DART was chosen for its automatic parameter estimation property. The only parameter that has to be specified is the number of materials to identify which is always 2 (element and background) for the case of KES imaging. This state-of-the-art parameter-free discrete reconstruction algorithm allows for a significant reduction of the number of acquired projections. This, in addition to the single-shot approach, suggests that a low-dose 3D mapping of a contrast agent is in principle possible. In this work, considering the simulated entrance dose per projection, a total of 10.6 mGy was estimated for the case of the dataset with lowest statistics (60 projections). Therefore, it is reasonable to state that *in vivo* applications could be conceived.

#### 4. Conclusion

K-Edge Subtraction (KES) tomographic imaging using lab-based polychromatic sources and photon counting detectors is attractive, since conventional X-ray tubes can be considered instead of e.g. synchrotron sources. Provided that a X-ray photon counting detector with at least two counters (or thresholds) is available, a single-shot low-dose approach is feasible. This leads to perfectly co-registered images and potential *in vivo* applications without motion artifacts and the need of image registration. The energy resolution of the Pixie-III detector was found to be adequate for practical applications such as the volume quantification of clusters of Bannanoparticles in a breast cancer mouse model. Although limitations in image quality of CdTe photon-counting detectors still remain, a fundamental contribution comes from refined image pre-processing and discrete reconstruction. An easy-to-access lab-based technology for a routine 3D elemental mapping of a contrast medium ready for

further morphological quantification is therefore available.

**Acknowledgment**

The KEST project, funded by INFN - Istituto Nazionale di Fisica Nucleare (National Scientific Committee 5 for Technological and Interdisciplinary research) is acknowledged. Authors wish to thank the ESRF for the provision of the beamtime MI 1323, and Dr. H. Requardt for his support during data acquisition at ID17. A. Bravin thanks the Swedish Research Council (grant nr. X2015- 99x-22731-01-4) and the COST Action CA16122 BIONECA.

**Table 1.** Quantitative analysis of the FDK plus thresholding images compared to the SR reference image

	averaging over 10				averaging over 5				no averaging			
	TP [%]	FP [%]	FN [%]	$\epsilon$ [-]	TP [%]	FP [%]	FN [%]	$\epsilon$ [-]	TP [%]	FP [%]	FN [%]	$\epsilon$ [-]
720 proj.	7.08	0.47	4.34	0.60	4.45	0.15	6.97	0.38	1.72	0.06	9.70	0.15
180 proj.	3.68	0.23	7.75	0.32	1.98	0.09	9.44	0.17	0.28	0.02	11.14	0.02
60 proj.	0.80	0.03	10.62	0.07	0.36	0.01	11.06	0.03	0.02	0.01	11.41	0.01

**Table 2.** Quantitative analysis of the TVR-DART images compared to the SR reference image

	averaging over 10				averaging over 5				no averaging			
	TP [%]	FP [%]	FN [%]	$\epsilon$ [-]	TP [%]	FP [%]	FN [%]	$\epsilon$ [-]	TP [%]	FP [%]	FN [%]	$\epsilon$ [-]
720 proj.	6.67	1.62	4.75	0.51	6.81	1.89	4.62	0.51	6.41	1.38	5.02	0.50
180 proj.	6.98	2.16	4.44	0.51	6.07	0.47	5.35	0.51	6.06	1.21	5.36	0.48
60 proj.	6.15	0.76	5.28	0.50	7.59	1.08	3.84	0.61	6.77	1.46	4.66	0.53



References

[1] Thomlinson W, Elleaume H, Porra L and Suortti P 2018 *Physica Medica* **49** 58–76

[2] Baldelli P, Bravin A, Di Maggio C, Gennaro G, Sarnelli A, Taibi A and et al 2006 *Physics in Medicine and Biology* **51** 4233–4251

[3] Kulpe S, Dierolf M, Braig E, Gnther B, Achterhold K, Gleich B and et al 2018 *PLoS ONE* **13** e0208446

[4] Fredenberg E 2018 *Nuclear Instruments and Methods in Physics Research, Section A: Accelerators, Spectrometers, Detectors and Associated Equipment* **878** 74–87

[5] Taguchi K and Iwanczyk J 2013 *Medical physics* **40** 100901

[6] Ballabriga R, Alojy J, Campbell M, Frojdh E, Heijne E, Koenig T and et al 2016 *Journal of Instrumentation* **11** P01007–P01007

[7] Brombal L, Donato S, Brun F, Delogu P, Fanti V, Oliva P and et al 2018 *Journal of Synchrotron Radiation* **25** 1068–1077

[8] Roessl E and Proksa R 2007 *Physics in Medicine and Biology* **52** 4679–4696

[9] Schlomka J, Roessl E, Dorscheid R, Dill S, Martens G, Istel T, Bumer C, Herrmann C, Steadman R, Zeitler G, Livne A and Proksa R 2008 *Physics in Medicine and Biology* **53** 4031–4047

[10] Abudurexiti A, Kameda M, Sato E, Abderyim P, Enomoto T, Watanabe M, Hitomi K, Tanaka E, Mori H, Kawai T, Takahashi K, Sato S, Ogawa A and Onagawa J 2010 *Radiological Physics and Technology* **3** 127–135

[11] He P, Wei B, Cong W and Wang G 2012 *Medical Physics* **39** 6572–6579

[12] Huang K X, Deng Z, Xu X F and Xing Y X 2019 *Nuclear Science and Techniques* **30** 38

[13] Bellazzini R, Spandre G, Brez A, Minuti M, Pinchera M and Mozzo P 2013 *Journal of Instrumentation* **8** C02028

[14] Bellazzini R, Brez A, Spandre G, Minuti M, Pinchera M, Delogu P and et al 2015 *Journal of Instrumentation* **10** C01032

[15] Herman G and Kuba A 2003 *Proceedings of the IEEE* **91** 1612–1626

[16] Batenburg K, Bals S, Sijbers J, Kbel C, Midgley P, Hernandez J and et al 2009 *Ultramicroscopy* **109** 730–740

[17] Zhuge X, Palenstijn W and Batenburg K 2016 *IEEE Transactions on Image Processing* **25** 455–468

[18] Shu-Yen W, Ritman E and Higgins W 2002 *Computers in Biology and Medicine* **32** 55 – 71 ISSN 0010-4825

[19] Grabherr S, Hess A, Karolczak M, Thali M J, Friess S D, Kalender W A, Dirnhofer R and Djonov V 2008 *Microscopy Research and Technique* **71** 551–556

[20] Zagorchev L, Oses P, Zhuang Z, Moodie K, Mulligan-Kehoe M, Simons M and Couffignal T 2010 *Vascular Cell* **2** 7 ISSN 2045-824X

[21] Retif P, Pinel S, Toussaint M, Frochet C, Chouikrat R, Bastogne T and et al 2015 *Theranostics* **5** 1030–1044

[22] Brun F, Di Trapani V, Dreossi D, Longo R, Delogu P and Rigon L 2018 *Annual International Conference of the IEEE Engineering in Medicine and Biology Society* **2018** 5245–5248

[23] Brun F, Di Trapani V, Dreossi D, Rigon L, Longo R and Delogu P 2019 *IFMBE Proceedings* **68** 123–126

[24] Di Trapani V, Bravin A, Brun F, Dreossi D, Longo R, Mittone A and et al 2018 *Journal of Instrumentation* **13** C12008–C12008

[25] Di Trapani V, Bravin A, Brun F, Dreossi D, Longo R, Mittone A, Rigon L and Delogu P 2020 *Nuclear Instruments and Methods in Physics Research, Section A: Accelerators, Spectrometers, Detectors and Associated Equipment* **955** 163220

[26] Suortti P, Fiedler S, Bravin A, Brochard T, Mattenet M, Renier M, Spanne P, Thomlinson W, Charvet A, Elleaume H, Schulze-Briesse C and Thompson A 2000 *Journal of Synchrotron Radiation* **7** 340–347

[27] Mittone A, Manakov I, Broche L, Jarnias C, Coan P and Bravin A 2017 *Journal of Synchrotron Radiation* **24** 1226–1236

[28] Delogu P, Oliva P, Bellazzini R, Brez A, De Ruvo P, Minuti M and et al 2016 *Journal of Instrumentation* **11** P01015

[29] Feldkamp L, Davis L and Kress J 1984 *Journal of the Optical Society of America A: Optics and Image Science, and Vision* **1** 612–619

[30] Brun F, Accardo A, Kourousias G, Dreossi D and Pugliese R 2013 *International Symposium on Image and Signal Processing and Analysis, ISPA* 672–676

[31] Brun F, Kourousias G, Dreossi D and Mancini L 2009 *IFMBE Proceedings* **25** 926–929

[32] Oimoen M 2000 *Proc. of the Fourteenth International Conference on Applied Geologic Remote*

*Single-shot K-Edge Subtraction X-ray discrete Computed Tomography*

16

*Sensing* 311–319

[33] Poludniowski G, Landry G, Deblois F, Evans P and Verhaegen F 2009 *Physics in Medicine and Biology* **54** N433–N438 cited By 340

[34] Poludniowski G and Evans P 2007 *Medical Physics* **34** 2164–2174

[35] Poludniowski G 2007 *Medical Physics* **34** 2175–2186